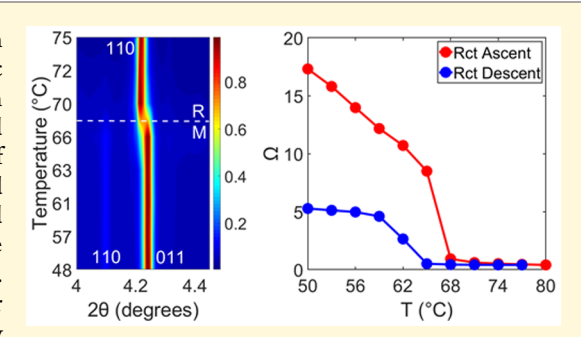


# Investigation of Conductivity and Ionic Transport of VO<sub>2</sub>(M) and VO<sub>2</sub>(R) via Electrochemical Study

Lisa M. Housel, Calvin D. Quilty, Alyson Abraham, Christopher R. Tang, Alison H. McCarthy, Genesis D. Renderos, Ping Liu, Esther S. Takeuchi, \*\*,†,‡,§ Amy C. Marschilok, \*,†,‡,§ and Kenneth J. Takeuchi\*, T, to

Supporting Information

ABSTRACT: Vanadium dioxides exist as a variety of polymorphs, each with differing structural and electrochemical capabilities. The monoclinic to rutile transition is an interesting system for study as the transition temperature is easily accessible at moderate temperature and corresponds to an increase in electrical conductivity by 2 orders of magnitude. The transition from monoclinic to rutile is characterized structurally herein using synchrotron-based X-ray diffraction and related to lithium-ion electrochemistry using electrochemical impedance spectroscopy and intermittent pulsatile galvanostatic discharge tests. The experimental results indicate a decrease in ohmic resistance for lithium-based cells tested under higher temperatures. Complementary



density functional theory calculations described the experimentally measured intercalation voltages and identified a possible Liinduced Li<sub>x</sub>VO<sub>2</sub>(M) to Li<sub>x</sub>VO<sub>2</sub>(R) phase transition during the discharging process rationalizing the favorable impact on the function of a lithium-based electrochemical cell. To our knowledge, this is the first observation of the metal-insulator transition of VO<sub>2</sub> in a full electrochemical cell.

#### ■ INTRODUCTION

The transition metal vanadium has proven useful in a variety of applications due to access to multiple oxidation states and coordination geometries where the applications range from energy related to catalysis<sup>1,2</sup> to biological applications.<sup>3-7</sup> Relevant to this manuscript are the experimental and theoretical investigations that have probed the VO2 metal to insulator transition. 8,9 At 68 °C, VO<sub>2</sub> undergoes a structural change from a monoclinic  $[VO_2(M)]$  to a rutile  $[VO_2(R)]$ phase, which is accompanied by an electrical conductivity increase of several orders of magnitude. 10,111 The changes to strain, 12,13 electric field, 14 and optical excitation 15 resulting from this phase transition have led to interest in thermo/electrochromatics and sensing applications. 16,17 Recent attempts to control the transition temperature have been made through controlled thin-film synthesis, 18 doping with tungsten<sup>19,20</sup> or titanium,<sup>21</sup> applying internal/external stress,<sup>22,23</sup> or changing microstructure and controlling crystallite size. 24,25 Other studies are centered on understanding the electronic and structural aspects of the phase transition at the microscopic level, 16 made possible by advanced characterizations such as ultrafast electron diffraction, <sup>26</sup> X-ray absorption spectroscopy, <sup>27</sup> and nanoscale imaging. <sup>28,29</sup>

Additionally, VO2 and other vanadium oxides are recognized as potential lithium-ion battery electrodes due to their high theoretical energy density, which arises from the variable oxidation state of vanadium.<sup>30</sup> Studies have used the VO<sub>2</sub>(B) polymorph as a cathode material<sup>31–34</sup> due to its high reported specific capacity (325 mAh/g)<sup>35</sup> relative to VO<sub>2</sub>(M) (<200 mAh/g) for one lithium equivalent at room temperature. 36,37 VO<sub>2</sub>(B) has edge-sharing VO<sub>6</sub> octahedra bilayers, which provide structural stability and facilitate lithium ion diffusion, while VO<sub>2</sub>(M) and VO<sub>2</sub>(R), have corner-sharing VO<sub>6</sub> octahedra that form a tunneled structure and result in anisotropic lithium-ion diffusion.

Recently, VO<sub>2</sub>(M) nanorod electrodes were fabricated that preferentially expose the (002) facet to improve the kinetics of lithium-ion diffusion. Compared to bulk VO<sub>2</sub>(M) nanoparticle electrodes, the oriented VO<sub>2</sub>(M) electrode delivered three times more reversible capacity vs Li/Li+ (320 mAh/g) and approached the specific capacity of VO<sub>2</sub>(B) electrodes (325 mAh/g).<sup>38</sup> Other approaches to improve VO<sub>2</sub>(M/R) electrodes include harnessing the higher electrical conductivity of the VO<sub>2</sub>(R) phase. Prior theoretical inquiries using ab initio calculations indicate the electronic structure is not significantly affected by the insertion of lithium ions at the initial stage,

Received: June 24, 2018 Revised: October 11, 2018 Published: October 12, 2018



7535

Department of Chemistry, Stony Brook University, Stony Brook, New York 11794, United States

<sup>\*</sup>Department of Materials Science and Chemical Engineering, Stony Brook University, Stony Brook, New York 11794, United States §Energy and Photon Sciences Directorate, Brookhaven National Laboratory, Upton, New York 11973, United States

suggesting electrical differences between  $VO_2(M)$  and  $VO_2(R)$  may be observable in an electrochemical cell.<sup>39</sup> However, the  $VO_2(R)$  phase is not stable at room temperature; therefore, accessing the  $VO_2(R)$  phase in an electrochemical cell must be done at temperatures above the  $VO_2(M)$  to  $VO_2(R)$  transition temperature.

In this manuscript, the electrical and structural changes that occur during the VO<sub>2</sub>(M) to VO<sub>2</sub>(R) transition as a function of temperature were determined. The VO<sub>2</sub> electrodes were incorporated into electrochemical cells to determine if the transition from monoclinic to rutile phase upon heating impacts impedance and functional electrochemistry. Through pulse testing, understanding of electron and ion transfer phenomena that occur during the  $VO_2(M-R)$  phase transition in an electrochemical cell was elucidated as a function of temperature. Complementary density functional theory calculations were performed to rationalize the experimentally measured intercalation voltages and a possible Li-induced Li<sub>x</sub>VO<sub>2</sub>(M) to Li<sub>x</sub>VO<sub>2</sub>(R) phase transition. This paper provides a foundation for investigating charge transport properties in polymorphic materials and sets a precedent for understanding the impact of phase changes on electrochemistry in a complex energy storage system.

#### **■** EXPERIMENTAL SECTION

**Synthesis.** Monoclinic vanadium(IV) oxide  $(VO_2(M))$  was synthesized using an approach similar to that previously reported. Briefly, vanadium pentoxide (Avantor) and oxalic acid (Spectrum Chemicals) reagents, in a 1:4 molar ratio, were reacted hydrothermally at 220 °C. The precursor material was then calcined at 750 °C under  $N_2$  to generate  $VO_2(M)$ .  $Li_{0.8}VO_2$  was synthesized by reacting stoichiometric amounts of  $VO_2(M)$  and  $LiBF_4$ .

Materials Characterization. Synchrotron X-ray diffraction data were collected at the National Synchrotron Light Source II (NSLS II) at Brookhaven National Laboratory, Beamline 28-ID-2. Temperature was varied using a nitrogen cryostream and confirmed externally with a thermocouple. The beam was calibrated to  $\lambda = 0.2372$  Å for the ascending temperature data set and to 0.2370 Å for the descending temperature data set of the unlithiated material and to  $\lambda = 0.1899 \text{ Å}$ for the lithiated material with lanthanum hexaboride used as the standard. The detector was a 16 in. amorphous silicon flat panel with a CsI scintillator. The resultant two-dimensional data were converted to a one-dimensional pattern using the Fit2D software. Rietveld refinement was executed with the GSAS II software. Routine characterization was performed on a Rigaku SmartLab X-ray diffractometer (Cu K $\alpha$ ,  $\lambda$  = 1.5406 Å) in a Bragg-Brentano configuration. Inductively coupled plasma-optical emission spectroscopy (ICP-OES) was executed using a Thermofisher iCAP 6300 series instrument.

Electrochemical Characterization. Impedance, pulse test, and galvanostatic intermittent titration technique (GITT) measurements were collected using coin type cells on a BioLogic VSP multichannel potentiostat. The two-electrode cell configuration contained a VO<sub>2</sub>(M) cathode, lithium metal anode, 1 M LiPF<sub>6</sub> in ethylene carbonate/dimethyl carbonate (3:7 v/v) electrolyte, and polypropylene separator. Electrochemical impedance spectroscopy (EIS) measurements were collected with a 10 mV sinus amplitude and a frequency range of 100 mHz to 100 kHz. Impedance data were fit using ZView fitting software, Version 3.5d. Initial impedance measurements were collected on cells with a cathode and no lithium metal or separator in the configuration. Pulse testing of two-electrode cells was executed with C/60 background current and pulse conditions of 20 mA/cm<sup>2</sup> for 10 s. Galvanostatic intermittent titration technique (GITT) tests used a discharge current of 14 mA/cm<sup>2</sup> for 10 min followed by a 1.5 h rest.

**Theory.** Spin-polarized DFT calculations were performed within the generalized gradient approximation (GGA) using the  $PW91^{42}$ 

pseudopotential as implemented in VASP.<sup>43</sup> A U correction term was used for V. The exact U values we used in this work were cited from fitting enthalpy of formation for binary oxides.<sup>44</sup> Specifically, the U value of 3.1 eV employed in the current calculation for vanadium was cited from a previous study by Ceder et al.<sup>45</sup> and was shown to well describe the experimentally measured behaviors of  $\text{Li}_x \text{VO}_2$  as lithium ion battery materials.<sup>39</sup>  $(\text{VO}_2)_8$  was employed to describe bulk  $\text{VO}_2$  in both rutile (R, space group P42/mnm) and monoclinic (M, space group P21/c) phases, where a plane-wave basis was utilized with a kinetic energy cutoff of 520 eV and a reciprocal-space k-point grid of  $3\times3\times9$  and  $6\times6\times3$ , respectively.  $\text{VO}_2$  cells were allowed to fully relax with the inserted Li ions. With such a setup, the lattice parameters optimized from the present DFT calculations agreed well with the experimental results using XRD (Table 1). Various models of

Table 1. Lattice Parameters for VO<sub>2</sub> from DFT Calculations and XRD Refinement

	$VO_2(R)$		$VO_2(M)$	
	XRD	DFT	XRD	DFT
a (Å)	4.55	4.61	5.75	6.05
b (Å)	4.55	4.61	4.53	4.52
c (Å)	2.85	2.91	5.38	5.43
$\alpha$ (deg)	90.0	90.0	90.0	90.0
$\beta$ (deg)	90.0	90.0	122.6	123.9
γ (deg)	90.0	90.0	90.0	90.0

Li $_x(VO_2)_8$  were constructed, and the corresponding formation energies were calculated as  $[E[(\text{Li}_x \text{VO}_2)_8] - 8xE(\text{Li}) - E[(\text{VO}_2)_8\text{-R}]]/8x$  in accordance with the previous study, <sup>46</sup> where E is the DFT-calculated total energy of a specific configuration; "x" is the lithiation (discharge) extent; and E(Li) is constant and is equal to the total energy of bulk metallic Li, which is assumed as the anode. The average intercalation voltage was calculated by  $-\{E[(\text{Li}_{x1}\text{VO}_2)_8] - E[(\text{Li}_{x2}\text{VO}_2)_8] - (x1 - x2)E(\text{Li})]/(x1 - x2)F$ , where F is Faraday's constant. The relative stability of a Li $_x\text{VO}_2$  system was expressed with respect to VO $_2$  and LiVO $_2$  as  $E[(\text{Li}_x\text{VO}_2)_8] - (1 - x)E[(\text{VO}_2)_8] - xE[(\text{LiVO}_2)_8]$ . Here  $E_f$  represents the energy cost to form Li $_x\text{VO}_2$  from VO $_2$  and Li bulk, while  $E_s$  corresponds to that from VO $_2$  and LiVO $_2$  bulk.

#### RESULTS

Synchrotron X-ray Diffraction. The VO<sub>2</sub>(M, <sup>47</sup> M2, <sup>48</sup> and R<sup>49</sup>) structures, shown in Figure 1, can be described as a chain of edge-sharing VO<sub>6</sub> octahedra where the chains are connected by corner linkages. VO<sub>2</sub>(M2) can be viewed as an intermediate of the  $VO_2(M)$  and  $VO_2(R)$  transition. In the case of  $VO_2(M)$ , the vanadium atoms are not entirely aligned along the longitudinal axis of the chain (Figure 1a); in VO<sub>2</sub>(M2) the vanadium atoms in half of the octahedra chains align leading to two distinct vanadium crystallographic sites (Figure 1b). In VO<sub>2</sub>(R), all the V<sup>4+</sup> ions are aligned and symmetrically equivalent (Figure 1c). Because of the vanadium alignment, the unit cell shifts from monoclinic for  $VO_2(M)$ , to monoclinic with a  $\beta$  angle of near 90° for VO<sub>2</sub>(M2), to tetragonal for VO<sub>2</sub>(R). Furthermore, as shown in Figure 1d–f, the octahedra chains of VO<sub>2</sub>(R) have a constant V-V bond of 2.872 Å (Figure 1f), while in VO<sub>2</sub>(M) there are alternating V-V bonds of 3.13 and 2.65 Å, respectively (Figure 1d). In VO<sub>2</sub>(M2), half of the chains have a constant V-V bond of 2.888 Å, while the other half alternate between 2.709 and 3.054 Å (Figure 1e). The alignment of the octahedral chains in  $VO_2(R)$  leads to the V 3d  $t_{2g}$  orbitals becoming degenerate and a decrease in energy of the  $e_q$  orbitals to near the Fermi level. This change in

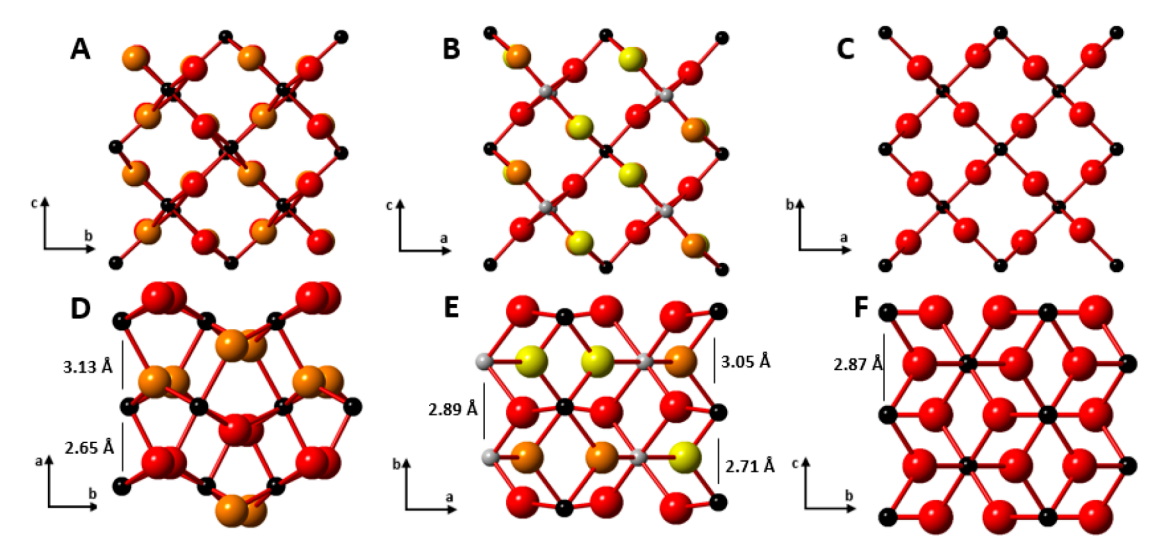


Figure 1. Crystal structures along the tunnel axis of (A) VO<sub>2</sub>(M), (B) VO<sub>2</sub>(M2), and (C) VO<sub>2</sub>(R). Black and gray indicate V, and red, orange, and yellow indicate O. Crystal structures along the lateral axis of (D) VO<sub>2</sub>(M), (E) VO<sub>2</sub>(M2), and (F) VO<sub>2</sub>(R) with select V–V distances identified.

electronic structure leads to dramatically higher conductivity upon transition to  $VO_2(R)$ .<sup>50</sup>

Synchrotron powder X-ray diffraction data, collected at room temperature, 48, 57, 61, 63, 66, 70, 72, and 75 °C, are shown in Figure 2a. Rietveld refinement was used to identify

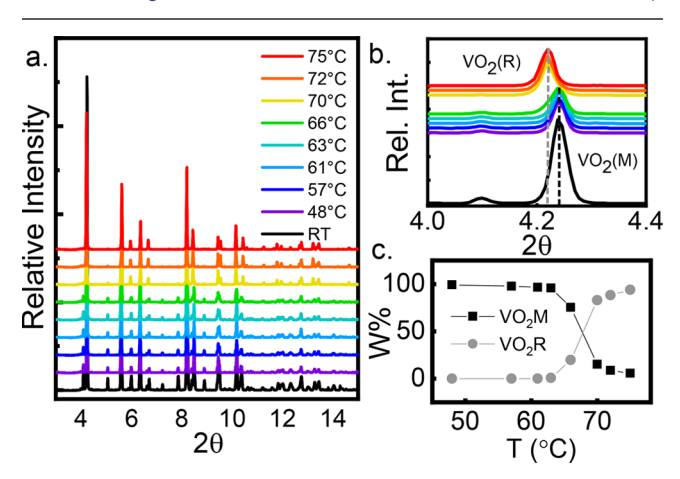


Figure 2. (a) X-ray diffraction patterns of  $VO_2$  as a function of temperature. (b) Highlighted two-theta range demonstrating peak shift associated with M to R transition. (c) Weight fractions of  $VO_2(M)$  and  $VO_2(R)$  as a function of temperature.

and quantify the phases present at each temperature (Figure S1). Refined lattice parameters (Tables S1–S2), thermal parameters (Table S3), and atomic positions (Table S4) are available in the Supporting Information, along with PDF card references for  $VO_2(M)$ ,  $VO_2(R)$ ,  $VO_2(M2)$ , and  $V_2O_5$ . The weight percentages of  $VO_2(M)$  and  $VO_2(R)$  as a function of increasing temperature are shown in Figure 2c.  $VO_2(M)$  is the primary phase at room temperature, confirming that  $VO_2(M)$  is produced from the hydrothermal synthesis followed by calcination. A small percentage of  $V_2O_5$  is noted (0.7%) and remains present throughout the temperature series (0.7–0.8%). Upon heating to 48 °C,  $VO_2(M)$  is the dominant phase (99.2%). At 57 °C,  $VO_2(M2)$  contributes 1.6% to the phase composition, which corresponds to a slight decrease in the  $VO_2(M)$  weight percent.

At 61 °C, the weight percent of VO<sub>2</sub>(M2) increases (2.5%) as  $VO_2(M)$  decreases (96.6%). At 63 °C, the  $VO_2(M2)$  weight percent levels (2.6%), VO<sub>2</sub>(M) decreases (95.5%), and  $VO_2(R)$  appears in small quantity (0.8%) for the first time. A dramatic change in composition occurs between 66 and 70 °C (Figure 2c). At 66 °C, there is a mixture of VO<sub>2</sub>(M) (75.5%) and  $VO_2(R)$  (19.8%) phases with  $VO_2(M)$  as the main phase. At 70 °C, VO<sub>2</sub>(R) (83.0%) is the dominant phase with  $VO_2(M)$  as the minor phase (15.1%). The weight percent of VO<sub>2</sub>(R) increases at 72 °C (88.1%) and 75 °C (93.9%) at the expense of VO<sub>2</sub>(M). The VO<sub>2</sub>(M-R) transition is observed by a peak shift from 4.24° to 4.22°, corresponding to the (011) and (110) planes for VO<sub>2</sub>(M) and VO<sub>2</sub>(R), respectively (Figures 2b and 3b). In addition, the (110) peak at  $4.1^{\circ}$  and the  $(10\overline{2})$  peak at  $5.1^{\circ}$  disappear once  $VO_2(R)$  is the majority phase (Figures 3b and 3c). The  $VO_2(M-R)$ conversion temperature range of 66-70 °C is consistent with previous reports. 52,53 It is noted that when the material is heated past the transition temperature and allowed to cool again the  $VO_2(M-R)$  transition shifts slightly to 64–61 °C. For the descending temperature data, X-ray diffraction patterns were collected at 76, 73, 70, 67, 64, 61, 58, 49, and ~21°C. There is no significant change in peak shape as temperature increases, suggesting that the crystallite size and microstrain are constant throughout this process.

 $VO_2(M2)$  is often observed as an impurity phase when  $VO_2(M)$  is heated and/or lithiated. As observed above,  $VO_2(M2)$  appears at 57 °C and can be detected in all the higher temperature patterns at 1–3% by weight. Interestingly, when the material was chemically lithiated with 0.8 equiv of Li<sup>+</sup> per  $V^{4+}$  ion and measured with XPD at room temperature, no  $VO_2(M2)$  peaks were detected. The material can be refined as pure  $VO_2(M)$  with a small lattice contraction; the Rietveld refinement, lattice parameters, atomic positions, and thermal parameters can be found in the Supporting Information (Figure S2, Tables S5, S6).

**Electrochemical Impedance Spectroscopy.** Cathode Configuration. A main outcome of the  $VO_2(M-R)$  transition is the reported change in material conductivity. The goal of this experiment was to quantify the impact on the impedance of  $VO_2$  in an environment resembling an electrochemical cell. Therefore, a one-electrode cell was constructed with a  $VO_2$ 

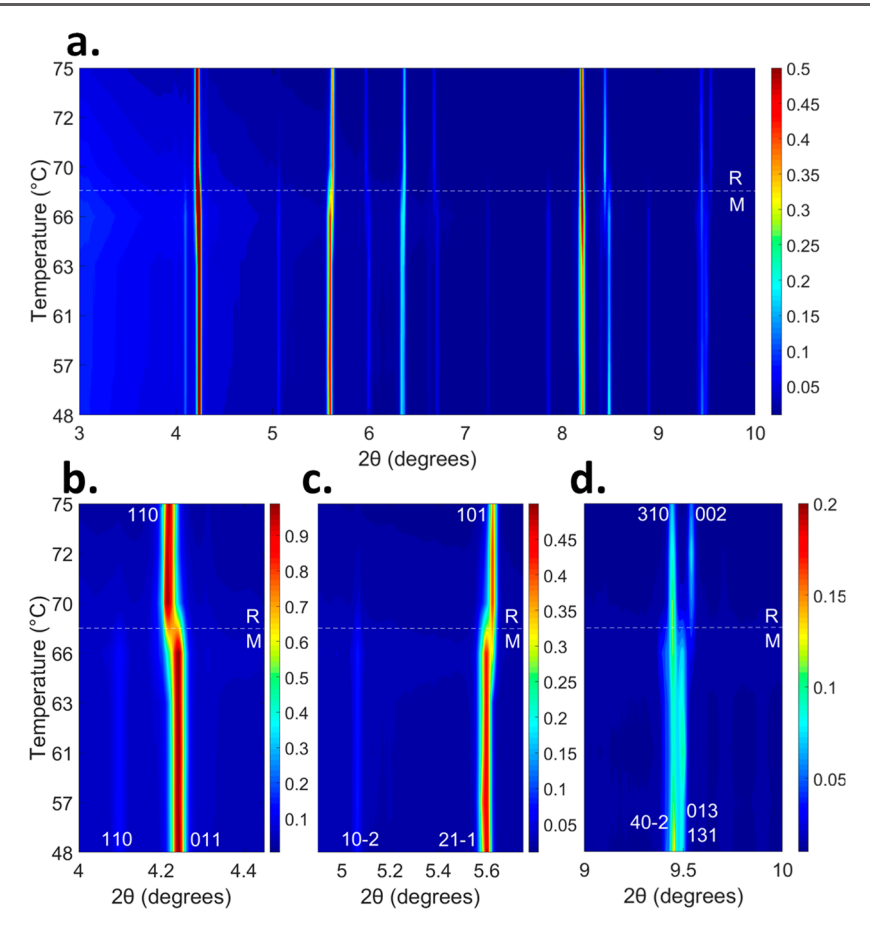


Figure 3. Temperature-dependent in situ X-ray powder diffraction patterns of VO<sub>2</sub> shown from (a)  $3-10^{\circ} 2\theta$ , (b)  $4-4.45^{\circ} 2\theta$ , (c)  $4.9-5.75^{\circ} 2\theta$ , and (d)  $9-10^{\circ} 2\theta$ .

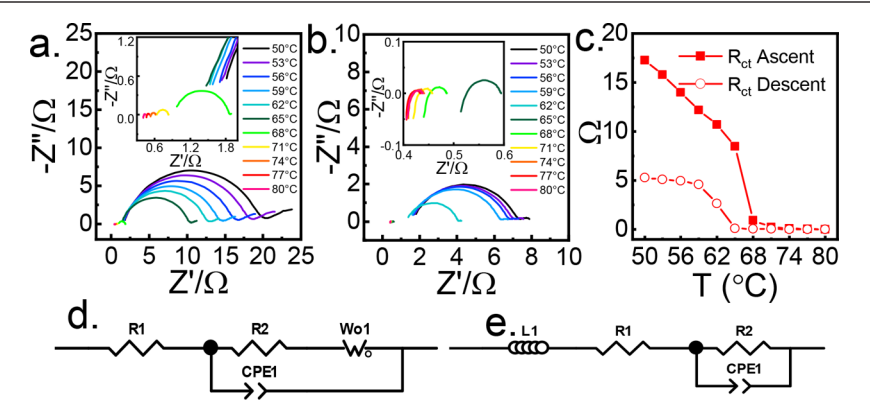


Figure 4. (a) AC impedance of VO<sub>2</sub> one-electrode cell as a function of increasing temperature. Inset: AC impedance at temperatures above 68 °C. (b) AC impedance of VO<sub>2</sub> one-electrode cell as a function of decreasing temperature. Inset: AC impedance at temperatures above 65 °C. (c) Charge transfer ( $R_{ct}$ ) resistance values as a function of temperature. Equivalent circuit models used for fitting (d) ≤65 °C upon ascending temperature, <65 °C upon descending temperature, where  $R_1$  and  $R_2$  represent  $R_{ohmic}$  and  $R_{ct}$  respectively.

electrode in the presence of Li<sup>+</sup>-containing electrolyte and the phase transition was monitored by measuring electrochemical impedance spectroscopy (Figure 4a and 4b). Synchrotron X-ray diffraction showed that the  $VO_2(M-R)$  transition as a function of increasing temperature and the  $VO_2(R-M)$  transition as a function of decreasing temperature do not occur at the same temperature. Thus, impedance collection for both ascending and descending temperature series is warranted.

The impedance of the one-electrode cell was modeled using a Randles circuit  $^{54}$  (Figure 4d), where circuit elements were used to represent different physical phenomena occurring in the cell.  $R_{\rm ohmic}$  represents resistance associated with electron transfer or ohmic resistance, while  $R_{\rm ct}$  is associated with charge transfer resistance within the VO $_2$  cathode. The presence of a semicircle in the Nyquist plot indicated a need for a capacitor in parallel with a resistor (RC component). A constant phase element (CPE1) was used instead of an ideal capacitor since the Nyquist plot was not a perfect semicircle.  $^{55}$  As temperature

increased, the semicircle of the Nyquist plot decreased, with the most dramatic reduction observed at 65–68 °C (Figure 4a). In the case of the lower-temperature data, a linear response was observed in the low-frequency range, as is commonly attributed to ion migration (diffusion). This linear response was not observed for the higher-temperature data. Therefore, a Warburg element (Wo1) was included to fit the lower temperature data (Figure 4d), but no Warburg element was included for the higher temperature data (Figure 4e).

At 50 °C,  $R_{\rm ohmic}$  and  $R_{\rm ct}$  were 1.662  $\pm$  0.004  $\Omega$  and 17.31  $\pm$ 0.05  $\Omega$ , respectively. Elevating the temperature by 3 °C reduced  $R_{\rm ohmic}$  and  $R_{\rm ct}$  to 1.606  $\pm$  0.004  $\Omega$  and 15.80  $\pm$  0.05  $\Omega$ , respectively. As temperature increased further,  $R_{\text{ohmic}}$  (Figure S3) and  $R_{ct}$  (Figure 4c) decreased in a linear fashion when plotted versus temperature until a noticeable drop in resistance was witnessed at 65-68 °C. Between 65 and 68 °C, Rohmic and  $R_{\rm ct}$  dropped from 1.359  $\pm$  0.003  $\Omega$  to 0.884  $\pm$  0.003  $\Omega$  and  $8.49 \pm 0.03 \Omega$  to  $0.966 \pm 0.002 \Omega$ , respectively. Visual changes in the Nyquist plots were observed from 65 to 68 °C. Therefore, a modified Randles circuit was used for the data collected at 68 °C and above (Figure 4e). At temperatures above 68 °C, the high frequency data had negative imaginary components, suggesting inclusion of an inductor circuit element as appropriate. At 71  $^{\circ}$ C,  $R_{\text{ohmic}}$  and  $R_{\text{ct}}$  were 0.605  $\pm$  0.003  $\Omega$  and 0.228  $\pm$  0.002  $\Omega$ , respectively. At 80 °C,  $R_{\rm ohmic}$ and  $R_{ct}$  were 0.4025  $\pm$  0.0004  $\Omega$  and 0.03550  $\pm$  0.0004  $\Omega$ , respectively. Equivalent circuit fitting results for the ascending cathode temperature series are in Table S7.

The dramatic change in resistance at 68 °C agreed with Xray diffraction data, suggesting a change from VO<sub>2</sub>(M) to VO<sub>2</sub>(R). X-ray diffraction results also showed that the evolution of VO<sub>2</sub>(R) occurred over a series of temperatures as opposed to an instantaneous conversion at 68 °C, where it was noted that below 61 °C only VO<sub>2</sub>(M) was present and at 75 °C  $VO_2(R)$  contributed over 90% to the material present. Therefore, the changes in  $R_{\rm ohmic}$  and  $R_{\rm ct}$  at 62 °C versus 74 °C most fully represent the resistance change associated with the  $VO_2(M)$  and  $VO_2(R)$  structures. As temperature increased, the  $VO_2(M)$  to  $VO_2(R)$  conversion resulted in a 0.883  $\pm$  0.003  $\Omega$ and  $10.61 \pm 0.04 \Omega$  decrease in  $R_{\text{ohmic}}$  and  $R_{\text{ct}}$ , respectively. Moreover, a linear decrease in resistance was noted as a function of temperature for both  $R_{\text{ohmic}}$  and  $R_{\text{ct}}$  before and after the major drop in resistance. Linear temperature dependence on conductivity of the VO<sub>2</sub> system has been noted in the literature before and after the conversion from monoclinic to rutile.56

As the cell was cooled from 80 to 68 °C (Figure 4b),  $R_{\text{ohmic}}$ and R<sub>ct</sub> increased linearly as a function of temperature and were determined via equivalent circuit shown in Figure 4e. Equivalent circuit fitting results for the descending oneelectrode cell temperature series are tabulated in Table S8. At 68 °C,  $R_{\rm ohmic}$  and  $R_{\rm ct}$  were 0.4345  $\pm$  0.0003  $\Omega$  and 0.0515  $\pm$ 0.0005  $\Omega$ , respectively. In contrast to the ascending series, a large increase in resistance was not observed upon cooling to 65 °C, where  $R_{\rm ohmic}$  and  $R_{\rm ct}$  remained low at 0.5037  $\pm$  0.0005  $\Omega$  and 0.0904  $\pm$  0.0005  $\Omega$ , respectively. Instead, the conversion was observed at 62 °C, where  $R_{\text{ohmic}}$  and  $R_{\text{ct}}$  were  $1.298 \pm 0.003 \ \Omega$  and  $2.64 \pm 0.02 \ \Omega$ , respectively. In the descending temperature series, upon cooling to 50 °C, R<sub>ohmic</sub> and  $R_{\rm ct}$  were 1.619  $\pm$  0.003  $\Omega$  and 5.27  $\pm$  0.02  $\Omega$  and lower than the original resistance values measured at 50 °C prior to heating and cooling the cell. In summary, impedance of the cathode configuration cell as a function of descending

temperature suggested that the  $VO_2(R)$  to  $VO_2(M)$  conversion occurred between 65 and 62 °C, which was consistent with X-ray diffraction data.

Electrochemical Impedance Spectroscopy. Two-Electrode Cell. The impedance of a lithium—VO $_2$  two-electrode cell was measured as a function of temperature to determine the impact of the VO $_2$ (M) to VO $_2$ (R) transition on a full cell. The equivalent circuit used to model impedance of the two-electrode cell configuration contained two resistor-capacitor (RC) components in addition to an ohmic resistor ( $R_{\rm ohmic}$ ) (Figure S4a). The sum of the resistor components from the RC pair represents charge transfer associated with both lithium anode and VO $_2$  cathode and was denoted as  $R_{\rm ct}$ . One equivalent circuit model was used for all temperatures. Tables S9 and S10 contain the equivalent circuit fitting results for the two-electrode cell as a function of ascending and descending temperature, respectively.

As temperature increased, the Nyquist plot semicircle decreased, with a noticeably larger reduction at 65–68  $^{\circ}$ C. Changes in  $R_{\rm ohmic}$  (Figure S4b) and  $R_{\rm ct}$  (Figure 5c) were also

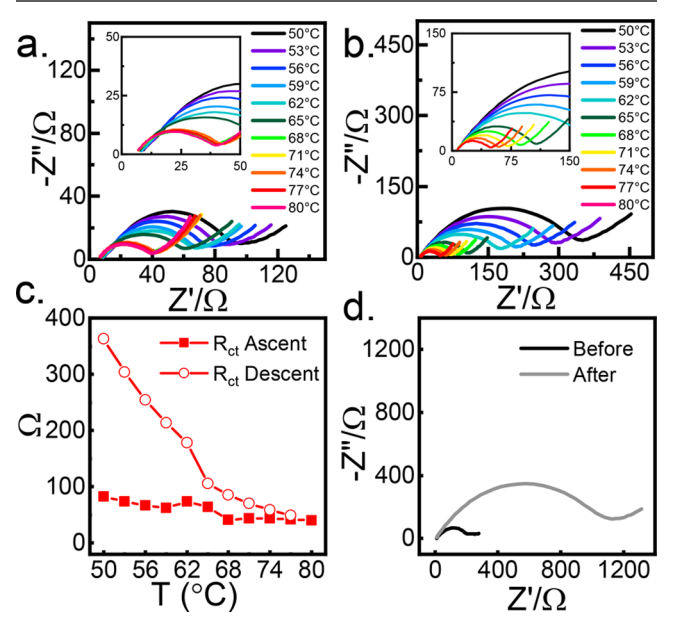


**Figure 5.** AC impedance of VO<sub>2</sub> two-electrode cell: (a) as a function of increasing temperature (inset: AC impedance of temperatures >65 °C); (b) as a function of decreasing temperature (inset: AC impedance of temperatures >65 °C); and (c) charge transfer ( $R_{\rm ct}$ ) resistance values as a function of temperature. (d) Impedance collected at 30 °C before and 24 h after the ascending and descending temperature series.

noticeable, suggesting the VO<sub>2</sub>(M) to VO<sub>2</sub>(R) transition occurred upon incorporation into a two-electrode cell (Figure 5a). At 50 °C,  $R_{\rm ohmic}$  and  $R_{\rm ct}$  were 8.19  $\pm$  0.03  $\Omega$  and 82.3  $\pm$  0.4  $\Omega$ . A 3 °C increase in temperature slightly reduced  $R_{\rm ohmic}$  (7.88  $\pm$  0.03  $\Omega$ ) and  $R_{\rm ct}$  (74.1  $\pm$  0.4  $\Omega$ ).  $R_{\rm ohmic}$  and  $R_{\rm ct}$  decreased steadily with increasing temperature from 50 to 68 °C until a more significant change at 65–68 °C, when  $R_{\rm ohmic}$  and  $R_{\rm ct}$  decreased from 6.4  $\pm$  0.1  $\Omega$  and 63  $\pm$  12  $\Omega$  to 5.11  $\pm$  0.07  $\Omega$  and 41  $\pm$  2  $\Omega$ , respectively. A continued gradual decrease in resistance was observed between 68 and 80 °C for  $R_{\rm ct}$  with no significant change in  $R_{\rm ohmic}$  in this temperature range. At 80 °C,  $R_{\rm ohmic}$  and  $R_{\rm ct}$  were 5.17  $\pm$  0.03  $\Omega$  and 39  $\pm$  2  $\Omega$ , respectively. Similar to the one-electrode cell, the two-

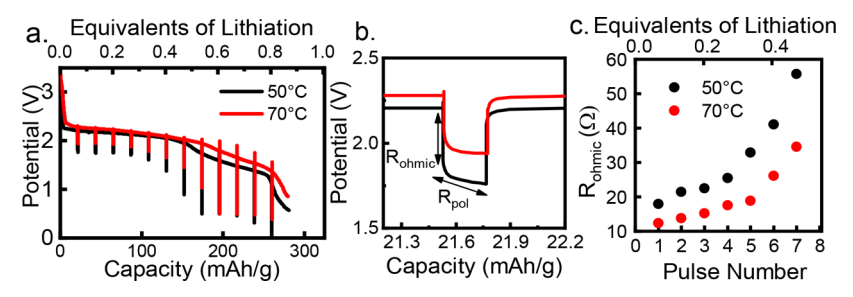


Figure 6. (a) Pulse test discharge curve of Li/VO<sub>2</sub> cell at 50 and 70  $^{\circ}$ C. (b) First pulse of pulse test. (c)  $R_{\rm ohmic}$  vs pulse number with corresponding equivalents of lithiation.

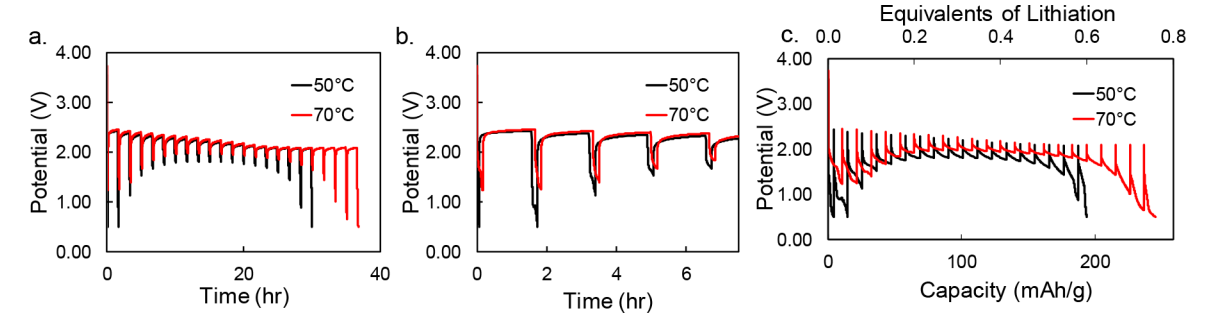


Figure 7. Galvanostatic intermittent titration technique (GITT). 14 mA/cm<sup>2</sup> discharge for 10 min with 1.5 h rest. (a) Potential vs time plot for complete discharge. (b) Potential vs time plot for initial 5 discharge steps. (c) Potential vs capacity for complete discharge with corresponding equivalents of lithiation.

electrode cell demonstrated its most significant change in resistance between 65 and 68 °C, suggesting the VO<sub>2</sub>(M) to VO<sub>2</sub>(R) transition occurred at this temperature, and was detectable in the presence of a lithium anode. Upon heating from 62 to 74 °C,  $R_{\rm ohmic}$  and  $R_{\rm ct}$  were reduced by 1.4  $\pm$  0.4  $\Omega$  and 31  $\pm$  10  $\Omega$ , respectively.

As the temperature was cooled from 80 to 71 °C (Figure 5b),  $R_{\rm ohmic}$  and  $R_{\rm ct}$  increased to 5.43  $\pm$  0.04  $\Omega$  and 70  $\pm$  4  $\Omega$ , respectively. The largest change in  $R_{\rm ct}$  occurred between 65 °C (106  $\pm$  3  $\Omega$ ) and 62 °C (178  $\pm$  2  $\Omega$ ), while for  $R_{\rm ohmic}$  the most significant change was observed between 68 °C (5.21  $\pm$  0.02  $\Omega$ ) and 62 °C (6.32  $\pm$  0.02  $\Omega$ ). Upon cooling to 50 °C,  $R_{\rm ohmic}$  (6.48  $\pm$  0.05  $\Omega$ ) was slightly smaller than that observed initially when measured at 50 °C prior to the heating and cooling series. Thus, the behavior and the trend upon cooling to 50 °C were consistent with the one-electrode cell. However, in the case of the two-electrode cell, the  $R_{\rm ct}$  (362  $\pm$  6  $\Omega$ ) after the heating/cooling series was much larger than  $R_{\rm ct}$  prior to the heating/cooling series.

The larger impedance of the two-electrode cell after cooling suggests that reactions other than  $VO_2(R)$  to  $VO_2(M)$ conversion affected the impedance of the two-electrode cell after the temperature testing. A possible explanation for the large increase in charge transfer resistance is vanadium dissolution and deposition on the lithium metal anode. When vanadium dissolves, the vanadium ions in the electrolyte migrate to the anode and form a film that increases the resistance of the cell. A previous study compared two cells with lithium silver vanadium oxide cathode, where one cell contained a pristine lithium anode and the other contained a lithium anode coated with  $14 \mu g/cm^2$  of vanadium present on the anode surface.<sup>56</sup> Impedance data and equivalent circuit modeling showed that coating the lithium anode with vanadium increased R<sub>ct</sub> relative to the control where 24 h after cell construction  $R_{ct}$ 's for the vanadium coated and

control lithium cells were 90 and 45  $\Omega$ , and 120 h after construction the values were 2500 and 1400  $\Omega$ , respectively. In this work,  $R_{\rm ct}$  values for the two-electrode cell from impedance measurements before and after the temperature series at 30 °C were 203  $\pm$  11  $\Omega$  and 1103  $\pm$  9  $\Omega$ , respectively (Figure 5d). ICP-OES of the dissolved lithium anodes after the temperature series detected a vanadium content equivalent to 1.26  $\mu {\rm g/cm^2}$  on the lithium anode.

**Functional Electrochemistry.** Pulse testing was conducted at 50 and 70 °C to demonstrate the effect of the  $VO_2(M)$  to  $VO_2(R)$  phase change on a functioning two-electrode  $Li/VO_2$  electrochemical cell (Figure 6a). In an operating electrochemical cell, there exists a difference between theoretical and operating (observed) potential due to resistances that occur on multiple levels within the cell. The operating potential (*E*) of an electrochemical cell is described by eq  $1^{57}$ 

$$E = E^{0} - [(n_{ct})_{a} + (n_{c})_{a}] - [(n_{ct})_{c} + (n_{c})_{c}] - iR_{i}$$
 (1)

where  $E^0$  is the standard potential;  $(\eta_{\rm ct})_{\rm a}$  and  $(\eta_{\rm ct})_{\rm c}$  are activation or charge transfer polarization;  $(\eta_{\rm c})_{\rm a}$  and  $(\eta_{\rm c})_{\rm c}$  are concentration or mass transfer polarization; i is the operating current; and  $R_{\rm i}$  is the internal resistance of the cell. The polarization and resistance components that affect operating voltage can be quantified using a pulse test.  $R_{\rm ohmic}$  refers to the internal resistance of the cell and specifically related to the  $iR_{\rm i}$  term, while  $R_{\rm pol}$  represents charge and mass transfer polarization from both anode and cathode (Figure 6b).

The initial voltage drop of the pulse represents ohmic resistance ( $R_{\rm ohmic}$ ) and is the feature selected to correlate with the phase transition of VO<sub>2</sub>(M) to VO<sub>2</sub>(R). The first pulse conducted at 50 and 70 °C is shown in Figure 6b.  $R_{\rm ohmic}$  was plotted versus pulse number for the first seven pulses (Figure 6c), and the  $R_{\rm ohmic}$  of each pulse is consistently higher at 50 °C than 70 °C. Moreover, the difference in  $R_{\rm ohmic}$  between the 50

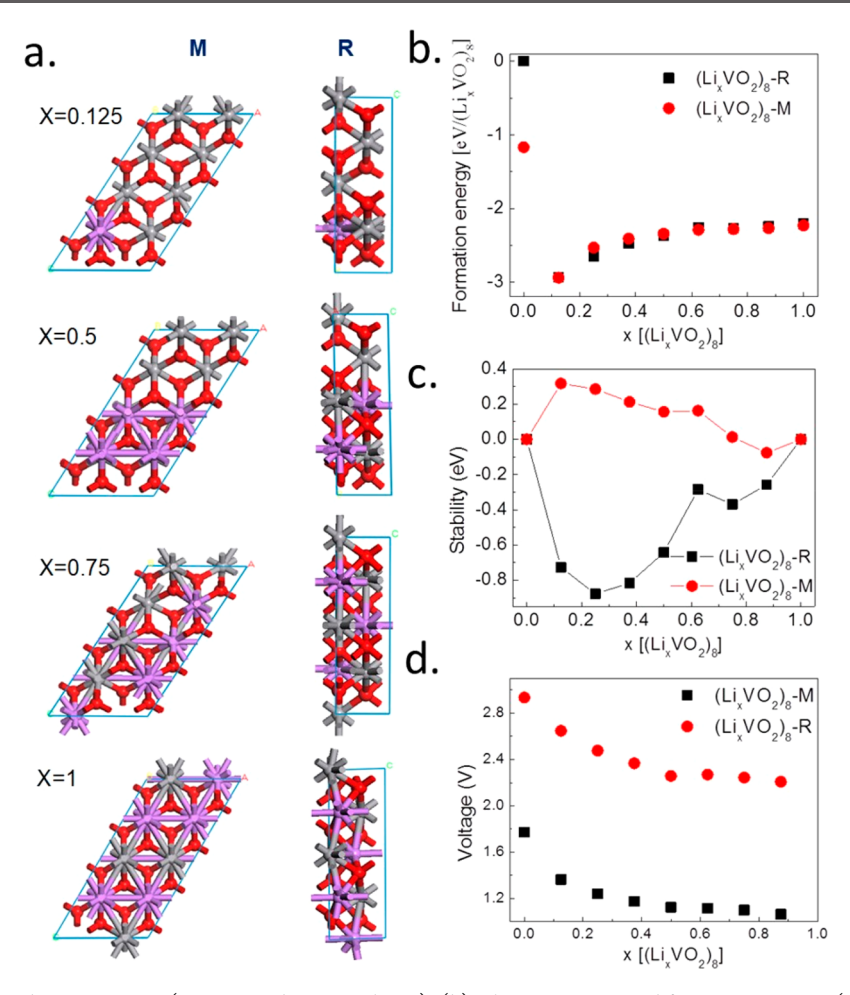


Figure 8. (a)  $\text{Li}_x \text{VO}_2$  intermediate structures (gray: V; red: O; purple: Li). (b) The DFT-estimated formation energy, (c) stability, and (d) average intercalation voltage for  $\text{Li}^+$  ion intercalation into  $\text{VO}_2(R)$  and  $\text{VO}_2(M)$ .

and 70 °C cell increased as a function of pulse number. At pulse 1, the 50 °C pulse was 5.7  $\Omega$  higher than the 70 °C pulse. At pulse 7, the 50 °C pulse was 21  $\Omega$  higher than the 70 °C pulse. In summary, a consistent reduction of  $R_{\rm ohmic}$  when tested at 70 °C was observed relative to that at 50 °C, consistent with the VO<sub>2</sub>(M) and VO<sub>2</sub>(R) transition and an electrical conductivity effect. At pulses 1–7, the  $R_{\rm pol}$  contribution remained similar between the 50 and 70 °C cells (Figure S5).

Galvanostatic intermittent titration technique (GITT) was employed to test the 50 and 70 °C cells under a smaller current and longer discharge time relative to the pulse test. Throughout the discharge, the 50 °C cell demonstrated a lower potential at each depth of discharge (Figure 7a and 7c). The difference in potential between the 50 and 70 °C cell was most significant early in the discharge as shown in Figure 7b. In addition, the 70 °C cell delivered more capacity (245 mAh/g) than the 50 °C cell (194 mAh/g) upon completion of the GITT test. The pulse and GITT tests showed the 50 °C cell has a lower operating potential (higher internal resistance) at each depth of discharge relative to the 70 °C cell. Thus, the pulse and GITT tests support the initial hypothesis that conversion to VO<sub>2</sub>(R) can impact the functional electrochemistry of a VO<sub>2</sub> electrochemical cell.

**Theory.** The DFT calculations started with the nonlithiated VO<sub>2</sub> crystal structures in both monoclinic and rutile phases. As shown in Table 1, the DFT-optimized lattice parameters are in good agreement with the values measured experimentally. Our

calculations show that  $VO_2(R)$  is less stable than  $VO_2(M)$  by  $1.17~eV/(Li_xVO_2)_8$ . This agrees with the experiment, showing the preference for the  $VO_2(M)$  phase at lower temperature. Upon  $Li^+$  intercalation, the octahedral vacancy is preferred, where the  $Li^+$  ion is bonded to six O atoms (Figure 8a), consistent with the previous DFT calculations.<sup>39</sup> The sequence of intercalation depends on the position of existing  $Li^+$  ions in the bulk, where the octahedral vacancy adjacent to the site occupied by one  $Li^+$  is always preferred. The filling of  $Li^+$  ions results in the structural distortion and breaking of local symmetry, which activates the neighboring octahedral vacancies to stabilize the inserted  $Li^+$ . In addition, the lithiation also favors a transition in phase preference from M to R

At x = 0.125, the difference in formation energy between M and R decreases to  $0.01 \text{ eV}/(\text{Li}_x \text{VO}_2)_8$  (Figure 8b). Specifically, x = 0.25 is the critical point, where the R phase is  $0.1 \text{ eV}/(\text{Li}_x \text{VO}_2)_8$  more stable than the M phase. Such a thermodynamic preference for the R phase may drive the M  $\rightarrow$  R transition. By comparison, the driving force for M  $\rightarrow$  R transition is lower at higher states of lithiation, x = 0.375 and 0.5, where it decreases to  $0.07 \text{ eV}/(\text{Li}_x \text{VO}_2)_8$  and  $0.03 \text{ eV}/(\text{Li}_x \text{VO}_2)_8$ , respectively. At 0.5 < x < 1, the M phases of  $\text{Li}_x \text{VO}_2$  are slightly more stable than the corresponding R phases by less than  $0.03 \text{ eV}/(\text{Li}_x \text{VO}_2)_8$ , which is not significant enough to initiate the phase transition. Based on these results, the Li intercalation at early stage of x = 0.25 likely contributes to the

 $M \rightarrow R$  phase transformation. Once the  $M \rightarrow R$  transition occurs, it is likely to remain in the R phase upon further lithiation to x = 1.

By definition (see Experimental section), the formation energy (Figure 8b) for both phases is expressed with the same reference: VO<sub>2</sub>(R) bulk and metallic Li bulk: that is, the energetic cost to form Li<sub>x</sub>VO<sub>2</sub> from VO<sub>2</sub>(R) and Li metal. However, it is important to note that reference for the stability of Li<sub>2</sub>VO<sub>2</sub> (Figure 8c) is phase-dependent, and the value is strongly associated with not only x value but also the energetics of corresponding VO2 and LiVO2 bulk in the same phase. Thus, the difference in formation energy is reflected by the total energy of Li, VO2, which is modified in the case of stability depending on the variation in total energy of  $VO_2$  and  $LiVO_2$  as well as x value. As a result, the lower formation energy of  $\text{Li}_{0.125}\text{VO}_2(M)$  as compared to  $\text{VO}_2(M)$ (Figure 8b), for instance, does not necessarily correspond to a higher stability (Figure 8c) due to the highly stable conformation of VO2(M). The VO2(R) behaves very differently from VO<sub>2</sub>(M) in terms of stability. None of the Li<sub>x</sub>VO<sub>2</sub>(M) structures are thermodynamically as stable as VO<sub>2</sub>(M). The Li<sub>0.875</sub>VO<sub>2</sub>(M) is an exception, yet the corresponding increase in stability is only 0.07 eV compared to VO<sub>2</sub>(M). The VO<sub>2</sub>(M) phase is too stable to allow the Li<sup>+</sup> intercalation and form the stable intermediates under lithiation conditions. In contrast, the relatively lower stability of  $VO_2(R)$ favors the formation of stable  $Li_xVO_2(R)$ , in particular for x =0.25 and 0.375. The filling of octahedral vacancies by Li<sup>+</sup> ions in  $VO_2(R)$  results in the stabilization of the system, which is more significant than that of VO<sub>2</sub>(M).

On the basis of the DFT-determined intermediates  $\operatorname{Li}_x \operatorname{VO}_2$ , the average  $\operatorname{Li}^+$  intercalation voltage was estimated. As shown in Figure 8d, for both  $\operatorname{VO}_2(M)$  and  $\operatorname{VO}_2(R)$  the voltage decreases with increasing amounts of lithation (i.e., with increasing x values in  $\operatorname{Li}_x \operatorname{VO}_2$ ), consistent with the experimental observations (Figure 6a). In terms of magnitude, the DFT-estimated voltage for  $\operatorname{VO}_2(R)$  agrees reasonably well with the experimental values, in particular at x < 0.5, where the voltage drop represents the resistance associated with electron transfer in the cell, while a relatively larger difference is observed at x > 0.5.

Both DFT calculations and experiment show that the corresponding voltage for VO<sub>2</sub>(M) is lower than that of VO<sub>2</sub>(R) (Figures 6 and 8d). However, the difference in voltage between VO<sub>2</sub>(M) and VO<sub>2</sub>(R) estimated by DFT is much larger than that observed experimentally by comparing the results from the pulse tests at 50 and 70 °C. Such discrepancy may be associated with broader temperature effects on other components in the battery as well as a Li-induced  $M \rightarrow R$ phase transformation as predicted by the DFT calculations (Figure 8). Accordingly, the intercalation of Li<sup>+</sup> ions at 50 °C may result in some fraction of phase transformation from  $\text{Li}_x \text{VO}_2(M)$  to the energetically more favorable  $\text{Li}_x \text{VO}_2(R)$ . Therefore, the pulsatile discharge voltages observed at 50 and 70 °C can be rationalized by the DFT calculations, which would support the formation of Li<sub>r</sub>VO<sub>2</sub>(R) under both temperatures.

# SUMMARY

Through a combination of synchrotron X-ray diffraction, electrochemical impedance spectroscopy, and density function theory, the electrochemistry of the  $\operatorname{Li}_x \operatorname{VO}_2$  system as a function of temperature has been rationalized. To our knowledge, this is

the first observation of the metal-insulator transition of VO<sub>2</sub> in a full electrochemical cell. The percentages of  $VO_2(M)$  and VO<sub>2</sub>(R) phases as a function of increasing temperature were determined quantitatively using synchrotron powder X-ray diffraction data coupled with Rietveld refinement. At room temperature  $VO_2(M)$  is the dominant phase present. At 70 °C, VO<sub>2</sub>(R) was observed to be the dominant phase present, and at 75 °C it represented 94% of the total material. Electrochemical impedance spectroscopy was used to interrogate the material as a function of temperature where a dramatic decrease in resistance was noted at 68 °C consistent with the phase change from VO<sub>2</sub>(M) to VO<sub>2</sub>(R). The impact of this phase change on the electrochemical function of lithium anode electrochemical cells was determined through pulse tests at 50 °C and at 70 °C. Ohmic resistance determined from the voltage drop at the leading edge of the pulse was used to compare the performance and shows that the cells tested at 70 °C demonstrated lower ohmic resistance than those tested at 50 °C, consistent with the increased electrical conductivity associated with the VO<sub>2</sub>(M) to VO<sub>2</sub>(R) transition. Finally, DFT calculations were used to assist in rationalizing the observations. The DFT results described the experimentally measured intercalation voltage well and also identified the possibility of an energetically favored lithiation-induced  $\operatorname{Li}_{x}VO_{2}(M) \rightarrow \operatorname{Li}_{x}VO_{2}(R)$  phase transition during the discharge process rationalizing the experimental electrochemical observations at different temperatures. This study can serve as an example for linking fundamental material-based charge transport properties in polymorphic materials to electrochemical behavior in a complex energy storage system.

#### ASSOCIATED CONTENT

# **S** Supporting Information

The Supporting Information is available free of charge on the ACS Publications website at DOI: 10.1021/acs.chemmater.8b02665.

Fitting parameters for electrochemical impedance spectroscopy and synchrotron X-ray diffraction data (PDF)

## AUTHOR INFORMATION

## **Corresponding Authors**

\*E-mail: esther.takeuchi@stonybrook.edu (EST).
\*E-mail: amy.marschilok@stonybrook.edu (ACM).
\*E-mail: kenneth.takeuchi.1@stonybrook.edu (KJT).

## ORCID

Ping Liu: 0000-0001-8363-070X

Esther S. Takeuchi: 0000-0001-8518-1047 Amy C. Marschilok: 0000-0001-9174-0474 Kenneth J. Takeuchi: 0000-0001-8129-444X

#### Notes

The authors declare no competing financial interest.

## ACKNOWLEDGMENTS

This work was supported as part of the Center for Mesoscale Transport Properties, an Energy Frontier Research Center supported by the U.S. Department of Energy, Office of Science, Basic Energy Sciences via grant #DE-SC0012673. This research used resources, specifically beamline 28-ID-2, of the National Synchrotron Light Source II, a U.S. Department of Energy (DOE) Office of Science User Facility operated for the DOE Office of Science by Brookhaven National

Laboratory under Contract No. DE-SC0012704. DFT calculations were performed using computational resources at the Center for Functional Nanomaterials at Brookhaven National Laboratory, an Office of Science User Facility under Contract No. DE-SC0012704. The authors thank Diana Lutz for assistance with data analysis. A.A. acknowledges support from the Graduate Assistance in Areas of National Need (GAANN) Fellowship. E.S.T. acknowledges support as the William and Jane Knapp Chair of Energy and the Environment.

## REFERENCES

- (1) Weberski, M. P.; McLauchlan, C. C. Synthesis, reactivity, and X-ray structural characterization of a vanadium(III) oxidation precatalyst, (CpPOEtCo)VCl2(DMF). *Inorg. Chem. Commun.* **2007**, *10*, 906–909.
- (2) McLauchlan, C. C.; Weberski, M. P.; Greiner, B. A. Synthesis, catalytic activity, phosphatase inhibition activity, and X-ray structural characterization of vanadium scorpionate complexes, (Tpms)VCl2-(DMF) and (Tpms)VOCl(DMF). *Inorg. Chim. Acta* **2009**, 362, 2662–2666.
- (3) McLauchlan, C. C.; Peters, B. J.; Willsky, G. R.; Crans, D. C. Vanadium-phosphatase complexes: Phosphatase inhibitors favor the trigonal bipyramidal transition state geometries. *Coord. Chem. Rev.* **2015**, *301*, 163–199.
- (4) Tracey, A. S.; Willsky, G. R.; Takeuchi, E. S. Vanadium: Chemistry, Biochemistry, Pharmacology and Practical Applications. CRC Press: Boca Raton, Florida, USA, 2007.
- (5) Doucette, K. A.; Hassell, K. N.; Crans, D. C. Selective speciation improves efficacy and lowers toxicity of platinum anticancer and vanadium antidiabetic drugs. *J. Inorg. Biochem.* **2016**, *165*, 56–70.
- (6) Krzystek, J.; Ozarowski, A.; Telser, J.; Crans, D. C. High-frequency and -field electron paramagnetic resonance of vanadium-(IV, III, and II) complexes. *Coord. Chem. Rev.* **2015**, *301*, 123–133.
- (7) Crans, D. C.; Tarlton, M. L.; McLauchlan, C. C. Trigonal Bipyramidal or Square Pyramidal Coordination Geometry? Investigating the Most Potent Geometry for Vanadium Phosphatase Inhibitors. *Eur. J. Inorg. Chem.* **2014**, 2014, 4450–4468.
- (8) Morin, F. J. Oxides that show a metal-to-insulator transition at the Neel temperature. *Phys. Rev. Lett.* **1959**, *3*, 34–36.
- (9) Goodenough, J. B. The two components of the crystallographic transition in VO2. *J. Solid State Chem.* **1971**, *3*, 490–500.
- (10) Cao, J.; Fan, W.; Chen, K.; Tamura, N.; Kunz, M.; Eyert, V.; Wu, J. Constant threshold resistivity in the metal-insulator transition of VO2. *Phys. Rev. B: Condens. Matter Mater. Phys.* **2010**, 82, 241101.
- (11) Yang, Z.; Ko, C.; Ramanathan, S. Metal-insulator transition characteristics of VO2 thin films grown on Ge(100) single crystals. *J. Appl. Phys.* **2010**, *108*, 073708.
- (12) Cao, J.; Ertekin, E.; Srinivasan, V.; Fan, W.; Huang, S.; Zheng, H.; Yim, J. W. L.; Khanal, D. R.; Ogletree, D. F.; Grossman, J. C.; Wu, J. Strain engineering and one-dimensional organization of metal-insulator domains in single-crystal vanadium dioxide beams. *Nat. Nanotechnol.* **2009**, *4*, 732–737.
- (13) Yang, M.; Yang, Y.; Bin, H.; Wang, L.; Hu, K.; Dong, Y.; Xu, H.; Huang, H.; Zhao, J.; Chen, H.; Song, L.; Ju, H.; Zhu, J.; Bao, J.; Li, X.; Gu, Y.; Yang, T.; Gao, X.; Luo, Z.; Gao, C. Suppression of Structural Phase Transition in VO2 by Epitaxial Strain in Vicinity of Metal-insulator Transition. *Sci. Rep.* **2016**, *6*, 23119.
- (14) Stefanovich, G.; Pergament, A.; Stefanovich, D. Electrical switching and Mott transition in VO2. *J. Phys.: Condens. Matter* **2000**, 12, 8837–8845.
- (15) Cavalleri, A.; Tóth, C.; Siders, C. W.; Squier, J. A.; Ráksi, F.; Forget, P.; Kieffer, J. C. Femtosecond Structural Dynamics in VO2 during an Ultrafast Solid-Solid Phase Transition. *Phys. Rev. Lett.* **2001**, 87, 237401.
- (16) Whittaker, L.; Patridge, C. J.; Banerjee, S. Microscopic and Nanoscale Perspective of the Metal-Insulator Phase Transitions of

VO2: Some New Twists to an Old Tale. *J. Phys. Chem. Lett.* **2011**, 2, 745–758.

- (17) Gao, Y.; Luo, H.; Zhang, Z.; Kang, L.; Chen, Z.; Du, J.; Kanehira, M.; Cao, C. Nanoceramic VO2 thermochromic smart glass: A review on progress in solution processing. *Nano Energy* **2012**, *1*, 221–246.
- (18) Stone, K. H.; Schelhas, L. T.; Garten, L. M.; Shyam, B.; Mehta, A.; Ndione, P. F.; Ginley, D. S.; Toney, M. F. Influence of amorphous structure on polymorphism in vanadia. *APL Mater.* **2016**, *4*, 076103.
- (19) Asayesh-Ardakani, H.; Nie, A.; Marley, P. M.; Zhu, Y.; Phillips, P. J.; Singh, S.; Mashayek, F.; Sambandamurthy, G.; Low, K.-b.; Klie, R. F.; Banerjee, S.; Odegard, G. M.; Shahbazian-Yassar, R. Atomic Origins of Monoclinic-Tetragonal (Rutile) Phase Transition in Doped VO2 Nanowires. *Nano Lett.* **2015**, *15*, 7179–7188.
- (20) Asayesh-Ardakani, H.; Nie, A.; Zhu, Y.; Phillips, P. J.; Klie, R. F.; Banerjee, S.; Odegard, G. M.; Shahbazian-Yassar, R. Atomic Resolution Studies of W Dopants Effect on the Phase Transformation of VO2. *Microsc. Microanal.* **2016**, 22, 884–885.
- (21) Wu, Y.; Fan, L.; Liu, Q.; Chen, S.; Huang, W.; Chen, F.; Liao, G.; Zou, C.; Wu, Z. Decoupling the Lattice Distortion and Charge Doping Effects on the Phase Transition Behavior of VO2 by Titanium (Ti4+) Doping. *Sci. Rep.* **2015**, *5*, 9328.
- (22) Fan, L. L.; Chen, S.; Luo, Z. L.; Liu, Q. H.; Wu, Y. F.; Song, L.; Ji, D. X.; Wang, P.; Chu, W. S.; Gao, C.; Zou, C. W.; Wu, Z. Y. Strain dynamics of ultrathin VO(2) film grown on TiO(2) (001) and the associated phase transition modulation. *Nano Lett.* **2014**, *14*, 4036–4043.
- (23) Muraoka, Y.; Hiroi, Z. Metal-insulator transition of VO2 thin films grown on TiO2 (001) and (110) substrates. *Appl. Phys. Lett.* **2002**, *80*, 583–585.
- (24) Yoon, J.; Kim, H.; Chen, X.; Tamura, N.; Mun, B. S.; Park, C.; Ju, H. Controlling the Temperature and Speed of the Phase Transition of VO2Microcrystals. *ACS Appl. Mater. Interfaces* **2016**, *8*, 2280–2286.
- (25) Whittaker, L.; Jaye, C.; Fu, Z.; Fischer, D. A.; Banerjee, S. Depressed Phase Transition in Solution-Grown VO2 Nanostructures. *J. Am. Chem. Soc.* **2009**, *131*, 8884–8894.
- (26) Morrison, V. R.; Chatelain, R. P.; Tiwari, K. L.; Hendaoui, A.; Bruhács, A.; Chaker, M.; Siwick, B. J. A photoinduced metal-like phase of monoclinic VO<sub>2</sub> revealed by ultrafast electron diffraction. *Science* **2014**, *346*, 445–448.
- (27) Cavalleri, A.; Rini, M.; Chong, H. H.; Fourmaux, S.; Glover, T. E.; Heimann, P. A.; Kieffer, J. C.; Schoenlein, R. W. Band-selective measurements of electron dynamics in VO2 using femtosecond nearedge x-ray absorption. *Phys. Rev. Lett.* **2005**, *95*, 067405.
- (28) Qazilbash, M. M.; Brehm, M.; Chae, B.-G.; Ho, P.-C.; Andreev, G. O.; Kim, B.-J.; Yun, S. J.; Balatsky, A. V.; Maple, M. B.; Keilmann, F.; Kim, H.-T.; Basov, D. N. Mott Transition in VO2 Revealed by Infrared Spectroscopy and Nano-Imaging. *Science* **2007**, *318*, 1750–1753.
- (29) Donges, S. A.; Khatib, O.; O'Callahan, B. T.; Atkin, J. M.; Park, J. H.; Cobden, D.; Raschke, M. B. Ultrafast Nanoimaging of the Photoinduced Phase Transition Dynamics in VO2. *Nano Lett.* **2016**, *16*, 3029–3035.
- (30) Marschilok, A. C.; Schaffer, C. P.; Takeuchi, K. J.; Takeuchi, E. S. Carbon nanotube—metal oxide composite electrodes for secondary lithium-based batteries. *J. Compos. Mater.* **2013**, *47*, 41–49.
- (31) Rahman, M. M.; Wang, J.-Z.; Idris, N. H.; Chen, Z.; Liu, H. Enhanced lithium storage in a VO2(B)-multiwall carbon nanotube microsheet composite prepared via an in situ hydrothermal process. *Electrochim. Acta* **2010**, *56*, 693–699.
- (32) Ganganagappa, N.; Siddaramanna, A. One step synthesis of monoclinic VO2 (B) bundles of nanorods: Cathode for Li ion battery. *Mater. Charact.* **2012**, *68*, 58–62.
- (33) Popuri, S. R.; Artemenko, A.; Decourt, R.; Josse, M.; Chung, U. C.; Michau, D.; Maglione, M.; Villesuzanne, A.; Pollet, M. Structurally Restricted Phase Transitions in VO2(B) and Their Impact on Transport Properties. *J. Phys. Chem. C* 2015, 119, 25085–25092.

(34) Xiao, X.; Li, S.; Wei, H.; Sun, D.; Wu, Y.; Jin, G.; Wang, F.; Zou, Y. Synthesis and characterization of VO2(B)/graphene nanocomposite for supercapacitors. *J. Mater. Sci.: Mater. Electron.* **2015**, *26*, 4226–4233.

- (35) Tsang, C.; Manthiram, A. Synthesis of nanocrystalline VO2 and its electrochemical behavior in lithium batteries. *J. Electrochem. Soc.* **1997**, *144*, 520–524.
- (36) Muñoz-Rojas, D.; Baudrin, E. Synthesis and electroactivity of hydrated and monoclinic rutile-type nanosized VO2. *Solid State Ionics* **2007**, *178*, 1268–1273.
- (37) Ni, J.; Jiang, W.; Yu, K.; Sun, F.; Zhu, Z. Electrochemical performance of B and M phases VO2 nanoflowers. *Cryst. Res. Technol.* **2011**, *46*, 507–510.
- (38) Song, H. J.; Park, S.; Lee, C. W.; Hong, S.-H.; Choi, M.; Kim, J.-C.; Kim, D.-W.; Kim, B.-K. Enhanced Lithium Storage in Reduced Graphene Oxide-supported M-phase Vanadium(IV) Dioxide Nanoparticles. *Sci. Rep.* **2016**, *6*, 30202.
- (39) Kulish, V. V.; Koch, D.; Manzhos, S. Ab initio study of Li, Mg and Al insertion into rutile VO2: fast diffusion and enhanced voltages for multivalent batteries. *Phys. Chem. Chem. Phys.* **2017**, *19*, 22538–22545
- (40) Li, G.; Chao, K.; Peng, H.; Chen, K.; Zhang, Z. Low-Valent Vanadium Oxide Nanostructures with Controlled Crystal Structures and Morphologies. *Inorg. Chem.* **2007**, *46*, 5787–5790.
- (41) Johnson, D. *ZView for Windows*, 3.5d. http://www.scribner.com/software/68-general-electrochemistr376-zview-for-windows/(accessed April 01, 2018).
- (42) Perdew, J. P.; Wang, Y. Accurate and Simple Analytic Representation of the Electron-Gas Correlation-Energy. *Phys. Rev. B: Condens. Matter Mater. Phys.* **1992**, *45*, 13244–13249.
- (43) Kresse, G.; Furthmuller, J. Efficient iterative schemes for ab initio total-energy calculations using a plane-wave basis set. *Phys. Rev. B: Condens. Matter Mater. Phys.* **1996**, *54*, 11169–11186.
- (44) Jain, A.; Hautier, G.; Moore, C. J.; Ping Ong, S.; Fischer, C. C.; Mueller, T.; Persson, K. A.; Ceder, G. A high-throughput infrastructure for density functional theory calculations. *Comput. Mater. Sci.* **2011**, *50*, 2295–2310.
- (45) Mueller, T.; Hautier, G.; Jain, A.; Ceder, G. Evaluation of Tavorite-Structured Cathode Materials for Lithium-Ion Batteries Using High-Throughput Computing. *Chem. Mater.* **2011**, 23, 3854–3862.
- (46) Guo, H.; Zhang, Y.; Marschilok, A. C.; Takeuchi, K. J.; Takeuchi, E. S.; Liu, P. A first principles study of spinel ZnFe2O4 for electrode materials in lithium-ion batteries. *Phys. Chem. Chem. Phys.* **2017**, *19*, 26322–26329.
- (47) Andersson, G.; et al. Studies on Vanadium Oxides. I. Phase Analysis. Acta Chem. Scand. 1954, 8, 1599–1606.
- (48) Galy, J.; Miehe, G. Ab initio structures of (M2) and (M3) VO2 high pressure phases. *Solid State Sci.* **1999**, *1*, 433–448.
- (49) Hoekstra, H. R.; Siegel, S.; Gallagher, F. X. Reaction of Platinum Dioxide with Some Metal Oxides. In *Platinum Group Metals and Compounds*; American Chemical Society: Washington D.C., 1971; Vol. 98, pp 39–53.
- (50) Eyert, V. The metal-insulator transitions of VO2: a band theoretical approach. *Ann. Phys.* (*Berlin, Ger.*) **2002**, *11*, 650–702.
- (51) Andersson, G.; et al. Vanadium oxides. II. The crystal structure of vanadium dioxide. *Acta Chem. Scand.* **1956**, *10*, 623–628.
- (52) Rogers, K. D. An X-ray diffraction study of semiconductor and metallic vanadium dioxide. *Powder Diffr.* **1993**, *8*, 240–244.
- (53) Kim, B.-J.; Lee, Y. W.; Chae, B.-G.; Yun, S. J.; Oh, S.-Y.; Kim, H.-T.; Lim, Y.-S. Temperature dependence of the first-order metal-insulator transition in VO2 and programmable critical temperature sensor. *Appl. Phys. Lett.* **2007**, *90*, 023515.
- (54) Randles, J. E. B. Kinetics of rapid electrode reactions. *Discuss. Faraday Soc.* **1947**, *1*, 11–19.
- (55) Jin, Y.; Gerhardt, R. A. Fabrication and simulation of semi-transparent and flexible PMMA/ATO conductive nanocomposites obtained by compression molding at different temperatures and pressures. AIP Adv. 2017, 7, 055004.

(56) Bock, D. C.; Marschilok, A. C.; Takeuchi, K. J.; Takeuchi, E. S. A Kinetics and Equilibrium Study of Vanadium Dissolution from Vanadium Oxides and Phosphates in Battery Electrolytes: Possible Impacts on ICD Battery Performance. *J. Power Sources* **2013**, 231, 219–225.

(57) Linden, D.; Reddy, T. B. *Handbook of Batteries*, 3rd ed.; The McGraw-Hill Companies, Inc.: New York, 2002.